nature medicine

Ammonia triggers neuronal disinhibition and seizures by impairing astrocyte potassium buffering

Vinita Rangroo Thrane[1–4,7], Alexander S Thrane[1–4,7], Fushun Wang[1], Maria L Cotrina[1], Nathan A Smith[1,5], Michael Chen[1], Qiwu Xu[1], Ning Kang[1], Takumi Fujita[1], Erlend A Nagelhus[1,2,6] & Maiken Nedergaard[1]

Ammonia is a ubiquitous waste product of protein metabolism that can accumulate in numerous metabolic disorders, causing neurological dysfunction ranging from cognitive impairment to tremor, ataxia, seizures, coma and death[1]. The brain is especially vulnerable to ammonia as it readily crosses the blood-brain barrier in its gaseous form, NH_3, and rapidly saturates its principal removal pathway located in astrocytes[2]. Thus, we wanted to determine how astrocytes contribute to the initial deterioration of neurological functions characteristic of hyperammonemia *in vivo*. Using a combination of two-photon imaging and electrophysiology in awake head-restrained mice, we show that ammonia rapidly compromises astrocyte potassium buffering, increasing extracellular potassium concentration and overactivating the Na^+-K^+-$2Cl^-$ cotransporter isoform 1 (NKCC1) in neurons. The consequent depolarization of the neuronal GABA reversal potential (E_{GABA}) selectively impairs cortical inhibitory networks. Genetic deletion of NKCC1 or inhibition of it with the clinically used diuretic bumetanide potently suppresses ammonia-induced neurological dysfunction. We did not observe astrocyte swelling or brain edema in the acute phase, calling into question current concepts regarding the neurotoxic effects of ammonia[3,4]. Instead, our findings identify failure of potassium buffering in astrocytes as a crucial mechanism in ammonia neurotoxicity and demonstrate the therapeutic potential of blocking this pathway by inhibiting NKCC1.

Ammonia neurotoxicity is an almost universal phenomenon that occurs in all animals, from fish to humans[5]. Ammonia homeostasis is particularly important in the brain as equimolar amounts of NH_4^+ are released with the excitotoxic neurotransmitter glutamate during neuronal firing[6]. In the brain, the enzyme that removes ammonia and glutamate, glutamine synthetase, has a higher affinity for ammonia than for glutamate[2,7]. In the rest of the body, ammonia detoxification is centralized to the liver, and liver disease frequently leads to encephalopathy that is thought to be due to ammonia neurotoxicity. Mortality in ammonia-handling disorders is primarily due to acute episodes of elevated blood ammonia (hyperammonemia), characterized by stupor, seizures and coma[1]. However, ammonia was also recently identified as an independent contributor to seizure development in epileptic children with normal liver function[8]. To understand this phenomenon, we here studied the direct effects of ammonia on intact nervous tissue. This approach avoided both the adaptive changes associated with chronic exposure and also any ammonia-independent pathology accompanying overt liver failure[9,10].

OTC deficiency is a childhood urea cycle disorder characterized by a reduced ability to metabolize ammonia to urea in the liver[1]. To induce acute ammonia intoxication, we injected awake adult ornithine transcarbamylase (OTC)-deficient (*Otc*$^{spf\text{-}ash}$) mice intraperitoneally (i.p.) with ammonia (ammonium chloride or ammonium acetate, 7.5 mmol kg^{-1}) (**Fig. 1a**)[9]. Shortly after the injection, we recorded a rapid increase in the extracellular ammonia concentration ($[NH_4^+]_o$) in the brain from 0.54 ± 0.18 mM to 4.83 ± 0.52 mM and in plasma from 0.32 ± 0.07 mM to 4.21 ± 0.59 mM (**Supplementary Fig. 1a**,**b**). We employed several behavioral measures to track the progression and severity of ammonia neurotoxicity. Automated video tracking revealed an early decrease in spontaneous movement (13.69 ± 1.48 m min^{-1} *Otc*$^{spf\text{-}ash}$ control versus 0.42 ± 0.22 m min^{-1} *Otc*$^{spf\text{-}ash}$ ammonia i.p.) (**Fig. 1b**). We also developed a phenotype severity score examining hyperacusis, imbalance, ataxia, tremor and level of consciousness that allowed us to track the rapid onset of neurological dysfunction (0.53 ± 0.28 *Otc*$^{spf\text{-}ash}$ control versus 9.00 ± 0.46 *Otc*$^{spf\text{-}ash}$ ammonia i.p.; a score of 0 represents normal function and 11 deep coma) (**Fig. 1c**)[9]. Similar to children with inborn OTC deficiency, the *Otc*$^{spf\text{-}ash}$ mice also displayed impaired learning at baseline compared to wild-type mice, tested using contextual fear conditioning. This finding probably reflects the baseline excess of $[NH_4^+]_o$ in *Otc*$^{spf\text{-}ash}$ mice (0.32 ± 0.07 mM in plasma) as compared to wild-type mice (0.074 ± 0.014 mM in plasma) (**Fig. 1d** and **Supplementary Fig. 1c**)[1,9,11].

In addition to cognitive, sensory and motor impairment, children with OTC deficiency typically develop myoclonic and other types of generalized seizures during episodes of hyperammonemia[1]. Around the time of weaning, *Otc*$^{spf\text{-}ash}$ mice also developed spontaneous myoclonic seizures, which are brief (<2 s) involuntary jerky movements

[1]Division of Glial Disease and Therapeutics, Center for Translational Neuromedicine, University of Rochester, Rochester, New York, USA. [2]Letten Centre, Institute for Basic Medical Sciences, University of Oslo, Oslo, Norway. [3]Centre for Molecular Medicine Norway, University of Oslo, Oslo, Norway. [4]Department of Ophthalmology, Haukeland University Hospital, Bergen, Norway. [5]Laboratory of Glial-Neuronal Interactions in Epilepsy, The Brain Institute, University of Utah, Salt Lake City, Utah, USA. [6]Department of Neurology, Oslo University Hospital, Oslo, Norway. [7]These authors contributed equally to this work. Correspondence should be addressed to A.S.T. (alexander.thrane@gmail.com).

Received 21 December 2011; accepted 17 October 2013; published online 17 November 2013; doi:10.1038/nm.3400

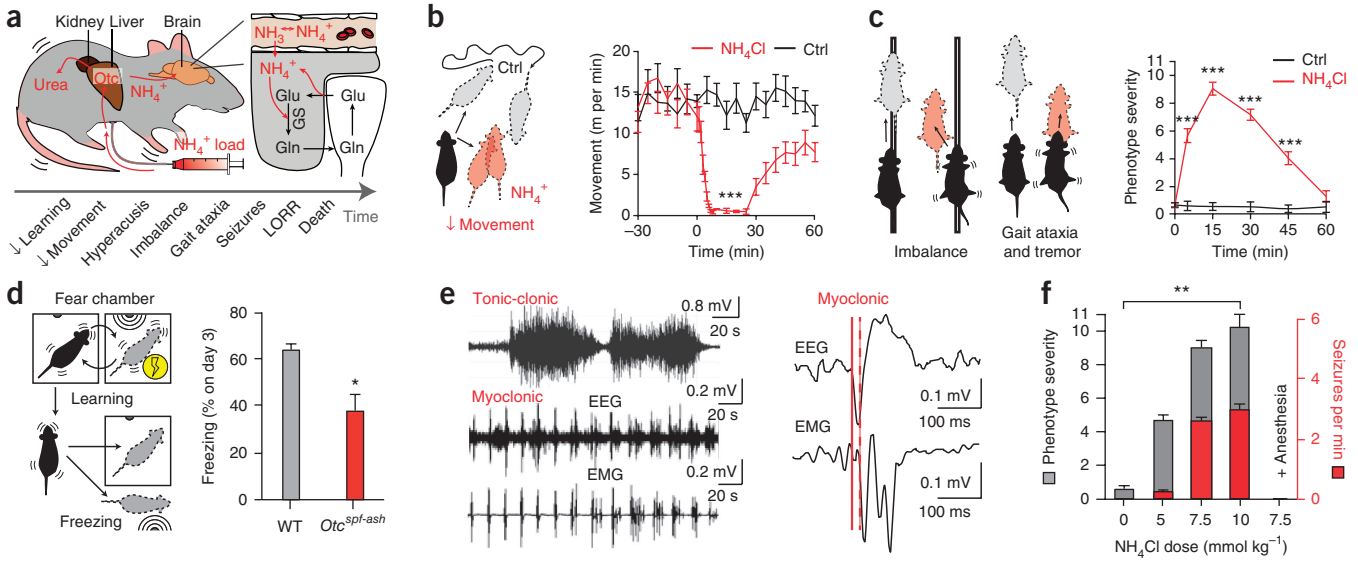

Figure 1 Ammonia causes severe neurological impairment and seizures. (**a**) Diagram showing *Otc*$^{spf\text{-}ash}$ mouse model of acute ammonia neurotoxicity. Otc, ornithine transcarbamylase; GS, glutamine synthetase; Glu, glutamate; Gln, glutamine; LORR, loss of righting reflex. (**b**) Automated movement analysis of *Otc*$^{spf\text{-}ash}$ mice given an i.p. ammonia injection (7.5 mmol kg^{-1}) and saline controls (Ctrl) (n = 5–8). (**c**) Phenotype severity score at different time points after ammonia (n = 8) or saline (n = 5) injection in *Otc*$^{spf\text{-}ash}$ mice at time 0. (**d**) Automated analysis of percentage time animal displays freezing during 5-min trials on day 3 of spatial fear conditioning comparing *Otc*$^{spf\text{-}ash}$ (n = 5) and wild-type (WT, n = 5) mice. (**e**) Representative electroencephalogram (EEG) and electromyogram (EMG) recordings of tonic-clonic and myoclonic seizures in ammonia-exposed *Otc*$^{spf\text{-}ash}$ animals (n = 10). (**f**) Phenotype severity (gray, left axis) compared to myoclonic seizure frequency (red, right axis) with increasing doses of ammonia in *Otc*$^{spf\text{-}ash}$ mice (n = 6 for each). Anesthetic, pooled data for isoflurane, ketamine with xylazine and urethane. $^{*}P < 0.05$, $^{**}P < 0.01$, $^{***}P < 0.001$. Data are shown as mean ± s.e.m.

caused by cortical seizure activity[9]. We injected ammonia to precipitate a more severe seizure phenotype and found that intermediate doses of ammonia (5–7.5 mmol kg^{-1}) triggered numerous myoclonic seizures, whereas a lethal dose (10 mmol kg^{-1}) induced longer lasting generalized tonic-clonic seizures (**Fig. 1e** and **Supplementary Video 1**). We found that the frequency of myoclonic seizures closely correlated with overall phenotype severity. The neurological phenotype was also entirely masked by anesthesia, emphasizing both the clinical relevance of our model and the need for recordings in awake animals (pooled data for isoflurane 1.5%, ketamine 0.12 mg per g body weight with xylazine 0.01 mg per g body weight and urethane 1.25 mg per g body weight) (**Fig. 1f**).

We next asked whether a primary dysfunction of astroglia might mediate the neurotoxic effects of ammonia. Astrocytes express glutamine synthetase, the primary enzyme necessary for ammonia detoxification, and are consequently subject to more than four times as much ammonia influx than any other cell type in the brain[12]. The current literature suggests that astrocyte swelling and brain edema are necessary for ammonia neurotoxicity, but consist mainly of *ex vivo* and post-mortem studies in the late stage of hepatic encephalopathy[2]. Using *in vivo* two-photon imaging, we instead found that i.p. ammonia injection was associated with a transient astrocyte shrinkage of 4.61 ± 0.72% and 5.04 ± 0.84% in wild-type and *Otc*$^{spf\text{-}ash}$ mice, respectively, lasting from 10 to 30 min after the injection (**Fig. 2a**,**b**)[4,13]. A lethal dose of ammonia was necessary to elicit brain edema (10 mmol kg^{-1} i.p. *in vivo*) and astrocyte swelling (50 mM *in situ*) (**Supplementary Fig. 1d**,**e**)[10]. Additionally, deletion of *Aqp4*, encoding the astrocyte water channel aquaporin-4, did not ameliorate the seizures, neurological dysfunction, brain edema or increase in ammonia (**Supplementary Fig. 1f**)[14,15]. We then tested the effect of ammonia neurotoxicity on the principal mode of astrocyte signaling: intracellular calcium transients. We found that injection of ammonia caused increased and desynchronized astrocyte calcium signaling, which was temporally correlated with seizure activity (calcium transient frequency 2.67 ± 0.36 mHz per cell *Otc*$^{spf\text{-}ash}$ control versus 9.03 ± 1.16 mHz per cell *Otc*$^{spf\text{-}ash}$ ammonia i.p.) (**Fig. 2c**, **Supplementary Videos 2** and **3** and **Supplementary Fig. 1g**–**i**)[16].

Since the widespread increase in astrocyte calcium signaling did not appear to be due to swelling[15], we next asked whether it might be linked to the interference of ammonia with potassium transport previously described in cell culture and the kidney[4,6,17,18]. Using NH_4^+ ion– and K^+ ion–sensitive microelectrodes (ISMs)[19] in awake *Otc*$^{spf\text{-}ash}$ mice, we found that i.p. ammonia injection increased the extracellular potassium concentration ($[K^+]_o$) in the cerebral cortex by 1.93 ± 0.19 mM (adjusted for ionic interference[17], **Fig. 2d**). As previous studies and our results indicate that the bulk of ammonia neurotoxicity occurs in cortical gray matter (**Supplementary Fig. 2a**)[2,20], we next applied ammonia directly on the cortex of awake wild-type mice. The ammonia dose was titrated in initial experiments to achieve a $[NH_4^+]_o$ increase to 5.82 ± 0.18 mM, which was similar to our observations from systemic toxicity and sufficient to reproduce the seizure phenotype (**Supplementary Table 1**). We also found that cortical ammonia intoxication in wild-type mice increased $[K^+]_o$ by 2.24 ± 0.17 mM from a resting level of 3.91 ± 0.27 mM (pooled control data) (**Fig. 2e** and **Supplementary Fig. 2b**–**d**). The $[K^+]_o$ increase following both i.p. injection and cortical superfusion of ammonia strongly correlated with (R^2 0.583 and 0.808, respectively) and consistently preceded (seizure onset 4.91 ± 0.35 min and 2.88 ± 0.20 min, respectively) myoclonic seizures and recovered upon washout as the neurological manifestations subsided (**Fig. 2f**). Conversely, the pH effects of ammonia in the cortex were mild and delayed and correlated poorly with clinical phenotype (**Supplementary Fig. 2e**).

Having established that ammonia increases $[K^+]_o$ sufficiently to cause neurological dysfunction *in vivo*, we wondered whether the

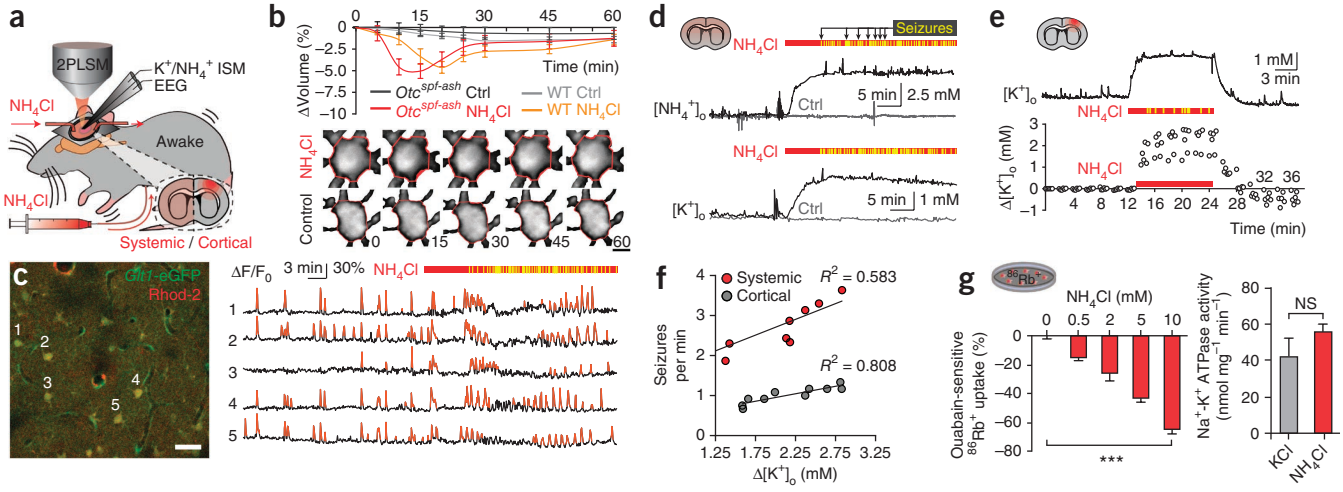

Figure 2 Ammonia compromises astroglial potassium buffering by competing for uptake. (**a**) Experimental setup for studying systemic and cortical ammonia neurotoxicity. 2PLSM, two-photon laser-scanning microscopy. (**b**) Top, volume analysis of eGFP-expressing astrocytes during ammonia neurotoxicity ($n = 12$ for each). Bottom, representative autothresholded images (red outline = volume at time 0). Scale bar, 5 µm. (**c**) Left, representative image of eGFP-expressing astrocytes loaded with calcium indicator rhod-2. Scale bar, 30 µm; depth, 100 µm. Right, corresponding rhod-2 intensity traces ($\Delta F/F_0$, eGFP-normalized) before and after a systemic ammonia load (red bar) in *Otc*$^{spf\text{-}ash}$ mouse. (**d**) Representative NH_4^+ (top) and K^+ (bottom) recordings following i.p. ammonia (red bar) or saline (control) injection in *Otc*$^{spf\text{-}ash}$ mice. (**e**) Representative K^+ trace (top) and scatterplot of all recordings (bottom, $n = 7$–10) after cortical application of ammonia (10 mM, red bar). (**f**) Linear regression of myoclonic seizure frequency on peak cortical $[K^+]_o$ during systemic and cortical ammonia neurotoxicity ($n = 8$–10). (**g**) Left, ouabain-sensitive rubidium ($^{86}Rb^+$) uptake in cultured astrocytes exposed to ammonia, normalized to vehicle ($n = 10$–23). Right, Na^+-K^+ ATPase activity measured in 15 mM KCl or NH_4Cl solution using a cell-free assay of astrocytes ($n = 4$ for each). (**h**) Representative recordings of K^+ (top) and myoclonic seizures (bottom) during cortical KCl application (red bar, 12.5 mM, $n = 6$). (**i**) Diagram of how anatomical (via astrocytic end-feet) and enzymatic (via glutamine synthetase, GS) trapping of ammonia in astrocytes compromises their ability to buffer potassium. Individual myoclonic seizures are indicated by yellow bars throughout. $^*P < 0.05$, $^{**}P < 0.01$, $^{***}P < 0.001$. NS, not significant. Data are shown as mean ± s.e.m.

excess NH_4^+ load on astrocyte membranes impairs potassium buffering by inhibiting transport or by directly competing for uptake. The gradients driving astrocyte uptake of potassium are largely dependent on Na^+-K^+ ATPase (NKA) activity, especially in the context of sustained $[K^+]_o$ elevations[17,21,22]. By incubating cultured wild-type astrocytes with biologically relevant concentrations of ammonia (0.5–10 mM), we observed a dose-dependent reduction in NKA-mediated (ouabain-sensitive) potassium analog rubidium ($^{86}Rb^+$) uptake (**Fig. 2g** and **Supplementary Fig. 2f**)[21]. We then substituted KCl with NH_4Cl in a cell-free assay derived from cultured astrocytes. We found that NH_4Cl alone was able to maintain normal NKA activity (**Fig. 2g**), which indicates that NH_4^+ competes with K^+ for transport. Notably, NH_4^+ and K^+ ions have a comparable hydrated radius and charge[6]. To test whether the $[K^+]_o$ increase alone is sufficient to reproduce the phenotype of ammonia neurotoxicity *in vivo*, we superfused KCl (12.5 mM) across the cortex of awake wild-type mice. The KCl superfusion increased $[K^+]_o$ by 2.37 ± 0.03 mM and caused the mice to develop myoclonic seizures on a similar timescale to those seen in wild-type mice exposed to cortical ammonia application (**Fig. 2h**). Combined, our observations indicate that ammonia short-circuits potassium transport in astrocytes and that the consequent increase in $[K^+]_o$ alone is sufficient to cause the neurological dysfunction. Given that astrocyte calcium transients potently stimulate NKA activity[21], hyperammonemia increases NKA activity[13] and increased NKA pumping causes cell shrinkage (3 Na^+ export versus 2 K^+ import), we speculate that our imaging observations represent compensatory changes in astrocytes to buffer the excess substrate ($[NH_4^+]_o$ and $[K^+]_o$) (**Fig. 2i**).

How does impaired astrocyte potassium buffering lead to neurological dysfunction and seizures? Previous *ex vivo* studies have generated numerous conflicting hypotheses about the effect of ammonia on neurotransmission[23–25]. To explore whether excess ammonia and potassium might cause neurological dysfunction by impairing cortical inhibition[26,27], we employed paired-pulse whisker stimulation in awake wild-type mice. This paradigm elicits two successive field excitatory post-synaptic potentials (fEPSPs), where the second fEPSP has lower amplitude primarily owing to the activation of cortical inhibitory networks (quantified by a paired-pulse ratio, PPR < 1)[28]. We found that cortical ammonia or potassium application impaired cortical inhibition, as illustrated by an increased PPR from 0.64 ± 0.13 (control) to 1.56 ± 0.24 (ammonia) and 1.48 ± 0.22 (potassium), which recovered to 0.61 ± 0.15 (washout) (**Fig. 3a**).

To further explore the link between impaired astrocyte potassium buffering and neuronal disinhibition we patched pyramidal neurons in acute cortical slices from wild-type mice. GABA is the main inhibitory neurotransmitter in the brain, and its inhibitory action on $GABA_A$ receptors is dependent on a hyperpolarized E_{GABA}[29]. Our initial experiments showed that adding 7 mM ammonia to the perfusate reproduced the increase in $[NH_4^+]_o$ and $[K^+]_o$ observed *in vivo* (3.67 ± 0.53 mM and 1.88 ± 0.13 mM, respectively) (**Fig. 3b**). Next, using whole-cell recordings and GABA application we found that ammonia depolarized E_{GABA} by +12.33 ± 3.66 mV (**Fig. 3c–e**). This effect

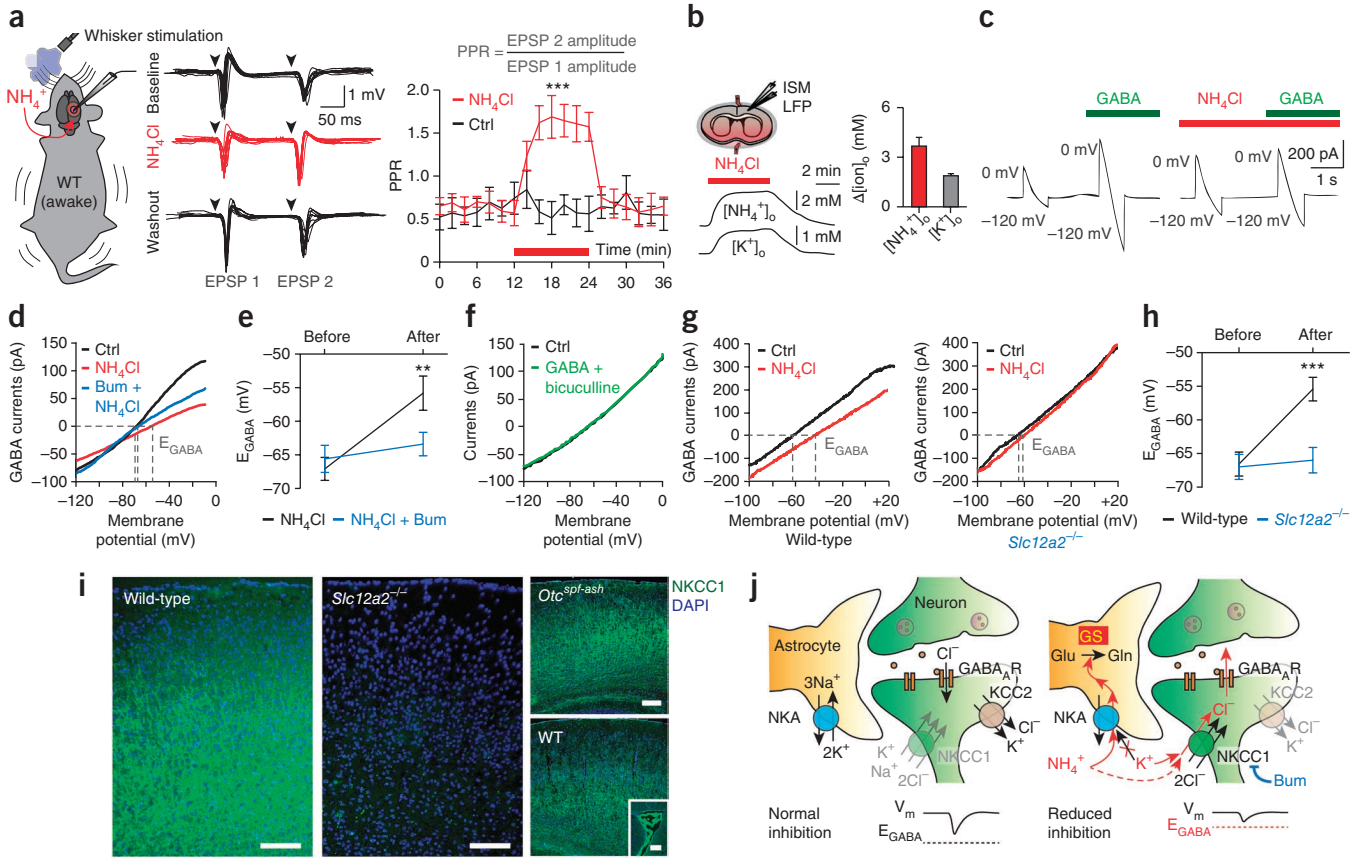

Figure 3 Excess ammonia and potassium depolarize E_{GABA} via NKCC1. (**a**) Left, diagram of whisker stimulation recordings. Middle, ten consecutive field EPSPs before, during (red) and after cortical ammonia application (10 mM) in WT mice. Right, PPR during cortical ammonia application (red bar) and in controls ($n = 10$ for each). (**b**) Left, diagram of cortical slice superfused with ammonia (top) and representative ion-sensitive microelectrode (ISM) recordings (bottom). LFP, local field potential. Right, change in ion concentration with 7.5 mM ammonia superfusion ($n = 9$–18). (**c**) Representative whole-cell current recordings from pyramidal neurons during ramp voltage, before and after GABA with or without ammonia application. (**d**) Current-voltage (I-V) curve comparing effect of ammonia ± bumetanide (Bum) on the currents induced by GABA applications ($n = 7$–11). (**e**) Mean E_{GABA} shift caused by ammonia with or without bumetanide ($n = 7$–11). (**f**) I-V curve of bicuculline and GABA co-application. (**g**) I-V curve for gramicidin perforated patch recordings before and after ammonia exposure in wild-type (left) and *Slc12a*$^{-/-}$ (right) mice ($n = 6$ or 7). (**h**) Mean ammonia-induced E_{GABA} shift in wild-type and *Slc12a*$^{-/-}$ mice ($n = 6$ or 7). (**i**) Immunofluorescence micrographs of wild-type, *Slc12a*$^{-/-}$ and *Otc*$^{spf\text{-}ash}$ mouse cortex labeled for NKCC1 (green) and nuclei (blue, DAPI). Inset shows choroid plexus. Scale bars, 100 µm. (**j**) Diagram showing the proposed mechanism for impaired astrocyte potassium buffering and neuronal E_{GABA} depolarization in ammonia neurotoxicity. $GABA_AR$, $GABA_A$ receptor; V_m, membrane potential. $^{**}P < 0.01$, $^{***}P < 0.001$. Data are shown as mean ± s.e.m.

was $GABA_A$ receptor dependent as the $GABA_A$ receptor antagonist bicuculline completely blocked the GABA-induced current (**Fig. 3f**), but was not associated with any significant change in neuronal resting membrane potential or input resistance[25].

A hyperpolarized E_{GABA} depends on the balance of chloride transport by NKCC1 and K^+-$2Cl^-$ cotransporter isoform 2 (KCC2)[29]. KCC2 deletion in mice is known to cause lethal seizures immediately after birth as a result of excess chloride import via NKCC1 (ref. 30). Conversely, deletion of the NKCC1 isoform gene *Slc12a2*, which is widely expressed in neurons and secretory epithelia, is associated with normal inhibitory GABA-ergic function[31,32]. NKCC1 is thus the principal chloride importer in neurons, and inhibition, knockout or knockdown of this transporter has been shown to treat temporal lobe, hypoglycemic, febrile and neonatal seizures by ensuring a hyperpolarized E_{GABA}[26,27,31–34]. Therefore, we next tested the therapeutic effect of the diuretic bumetanide, a highly specific NKCC1 inhibitor at low concentrations[26,27,35]. In our study, bumetanide treatment successfully prevented the depolarizing effect of ammonia on E_{GABA} (**Fig. 3d**,**e**). To ensure the molecular specificity of bumetanide, we also performed gramicidin-perforated patch recordings in constitutive NKCC1 knockout (*Slc12a2*$^{-/-}$) mice and wild-type (*Slc12a2*$^{+/+}$) littermates. NKCC1 deletion completely blocked the depolarizing effect of ammonia on E_{GABA} (+11.14 ± 1.22 mV in wild-type mice and +1.00 ± 1.07 mV in *Slc12a2*$^{-/-}$ mice) (**Fig. 3g**,**h**). In support of our observations, previous *in vivo*, *in situ* and *in vitro* work has shown that neurons exposed to elevated ammonia or potassium levels have increased intracellular chloride content[36,37]. Using immunohistochemistry of NKCC1-knockout and wild-type mice, we found that NKCC1 is expressed in adult cortex (**Fig. 3i**), confirming previous studies showing NKCC1 expression in adult brain, although at lower levels than in developing tissue[26,38]. We also observed no obvious differences in the expression pattern of NKCC1 between wild-type and *Otc*$^{spf\text{-}ash}$ mice. Taken together, our observations indicate that elevated $[NH_4^+]_o$ and $[K^+]_o$ promote overactivation of neuronal NKCC1, leading to a depolarization of E_{GABA}, impaired cortical inhibition and seizures (**Fig. 3j**).

We next explored potential treatments for ammonia neurotoxicity (**Fig. 4a**). It has previously been suggested that reducing ammonia

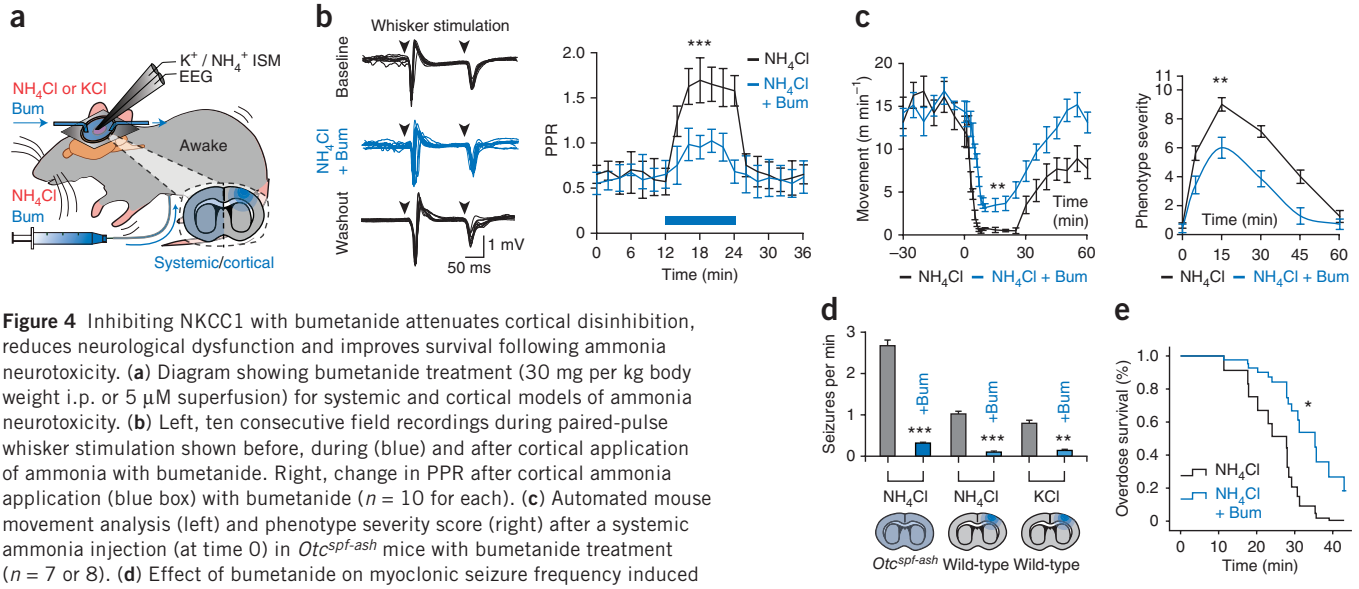

Figure 4 Inhibiting NKCC1 with bumetanide attenuates cortical disinhibition, reduces neurological dysfunction and improves survival following ammonia neurotoxicity. (**a**) Diagram showing bumetanide treatment (30 mg per kg body weight i.p. or 5 μM superfusion) for systemic and cortical models of ammonia neurotoxicity. (**b**) Left, ten consecutive field recordings during paired-pulse whisker stimulation shown before, during (blue) and after cortical application of ammonia with bumetanide. Right, change in PPR after cortical ammonia application (blue box) with bumetanide ($n = 10$ for each). (**c**) Automated mouse movement analysis (left) and phenotype severity score (right) after a systemic ammonia injection (at time 0) in *Otc*$^{spf\text{-}ash}$ mice with bumetanide treatment ($n = 7$ or 8). (**d**) Effect of bumetanide on myoclonic seizure frequency induced by ammonia and potassium neurotoxicity ($n = 6$–10). (**e**) Cox regression of *Otc*$^{spf\text{-}ash}$ mouse survival time after an ammonia overdose (10 mmol kg^{-1}, $n = 9$ or 10). $^{*}P < 0.05$, $^{**}P < 0.01$, $^{***}P < 0.001$. Data are shown as mean ± s.e.m.

influx into astrocytes by inhibiting glutamine synthetase can improve clinical outcome[3]. However, in awake intact animals we found that this strategy worsened the neurological phenotype by increasing the overall $[NH_4^+]_o$ and $[K^+]_o$ load on neurons (**Supplementary Fig. 3a–c**). Similarly, blocking ammonia import into glia via potassium transporters would also promote seizure development[17,22]. Instead, we hypothesized that inhibiting NKCC1 overactivation would be the most effective strategy, as this disrupts the vicious cycle of ammonia-induced disinhibition, excess neuronal firing and further potassium and ammonia release. Using the previously described paired-pulse paradigm, we found that bumetanide significantly improved cortical disinhibition when applied with either the cortical ammonia or potassium superfusion (PPR 0.88 ± 0.15 after ammonia and bumetanide application, PPR 0.59 ± 0.17 after washout of both, PPR 0.92 ± 0.18 after potassium and bumetanide) in wild-type mice (**Fig. 4b** and **Supplementary Fig. 3d**). NKCC1 inhibition also increased spontaneous movement in mice (from 0.42 ± 0.22 m min^{-1} to 3.17 ± 0.46 m min^{-1}), reduced the phenotype severity score (from 9.00 ± 0.46 to 6.00 ± 0.72) and decreased myoclonic seizure frequency (from 0.78 ± 0.05 seizures per minute to 0.13 ± 0.03 seizures per minute with cortical potassium, 1.02 ± 0.07 seizures per minute to 0.10 ± 0.02 seizures per minute with cortical ammonia and 2.66 ± 0.14 seizures per minute to 0.32 ± 0.02 seizures per minute with i.p. ammonia) (**Fig. 4c,d**). Moreover, survival of *Otc*$^{spf\text{-}ash}$ mice after an ammonia overdose (10 mmol kg^{-1}) increased by a factor of 3.87 (hazard rate ratio: 0.26, 95% confidence interval: 0.08–0.87) (**Fig. 4e**). These improvements were observed both when bumetanide was administered systemically (30 mg per kg body weight administered with ammonia i.p. in *Otc*$^{spf\text{-}ash}$ mice) and cortically (5 μM co-applied with ammonia on the cortex in wild-type mice). Bumetanide is also routinely used in clinical practice, has a favorable side-effect profile[35] and is estimated to have ~33% blood-brain barrier penetration[39]. Moreover, the therapeutic effect of bumetanide could not be attributed to a normalization of $[K^+]_o$, $[NH_4^+]_o$ or brain glutamine concentration, which were unaltered by the treatment in both wild-type and *Otc*$^{spf\text{-}ash}$ mice (**Supplementary Table 2** and **Supplementary Fig. 3e,f**).

In summary, we demonstrate that the immediate neurotoxic effects of ammonia are dependent on a dysfunction of glial and neuronal cells involving two crucial steps. First, ammonia competitively impairs astrocyte potassium buffering to such an extent that the resultant increase in $[K^+]_o$ (~2 mM) alone is sufficient to induce neurological dysfunction and seizures in awake animals. Second, excess $[NH_4^+]_o$ and $[K^+]_o$ promotes overactivation of neuronal NKCC1, which compromises inhibitory neurotransmission in the cortex. Deletion or selective inhibition of NKCC1 attenuates the neurological manifestations of acute ammonia intoxication. Additionally, our results bring into question the contribution of astrocyte swelling and brain edema to the onset of ammonia-induced neurological dysfunction. The use of awake mice proved crucial, as general anesthetics masked the clinical phenotype[16]. Our study thus provides a framework to further explore the clinical potential of NKCC1 inhibitors in treating the broad range of debilitating disorders of ammonia handling. Studies are also needed to investigate the role of this pathway in disorders characterized by chronic hyperammonemia and cognitive impairment.

METHODS

Methods and any associated references are available in the online version of the paper.

Note: Any Supplementary Information and Source Data files are available in the online version of the paper.

ACKNOWLEDGMENTS

We thank A.J. Cooper for discussion of the study, S. Kennedy for help with ^{1}H-NMR experiments, L.K. Bekar for help with electrophysiology, J. Chang for designing MatLab software, D. Wang for advice regarding electroencephalogram analysis, J.M. Wilson (University of Pennsylvania) for providing the *Otc*$^{spf\text{-}ash}$ mice, J.D. Rothstein (Johns Hopkins University) for providing *Glt1*-eGFP BAC transgenic mice and C. Nicholson and S. Hrabetova for advice on fabrication and use of ion-sensitive electrodes. This work was supported by the US National Institutes of Health (grants NS078304 and NS078167 to M.N. and F31NS073390 to N.A.S.), Research Council of Norway (NevroNor FRIMEDBIO grants to E.A.N.), European Commission FP7-ICT-9-601055 to E.A.N., the Molecular Life Science program at the University of Oslo, the Letten Foundation and the Fulbright Foundation.

AUTHOR CONTRIBUTIONS

V.R.T., A.S.T., E.A.N., M.L.C. and M.N. planned the project. V.R.T., A.S.T., M.L.C., E.A.N. and M.N. wrote the manuscript. V.R.T. and A.S.T. performed *in vivo* electrophysiology, imaging and data analysis. F.W., N.K. and Q.X. performed *in situ* electrophysiology. A.S.T., V.R.T. and M.C. performed behavioral experiments. A.S.T., V.R.T. and Q.X. performed *in situ* imaging. N.A.S. performed rubidium experiments. T.F. performed ATPase experiments. M.L.C. performed immunohistochemistry.

COMPETING FINANCIAL INTERESTS

The authors declare no competing financial interests.

1. Cagnon, L. & Braissant, O. Hyperammonemia-induced toxicity for the developing central nervous system. *Brain Res. Rev.* **56**, 183–197 (2007).
2. Cooper, A.J. 13N as a tracer for studying glutamate metabolism. *Neurochem. Int.* **59**, 456–464 (2011).
3. Butterworth, R.F. Pathophysiology of hepatic encephalopathy: a new look at ammonia. *Metab. Brain Dis.* **17**, 221–227 (2002).
4. Jayakumar, A.R. *et al.* Na-K-Cl Cotransporter-1 in the mechanism of ammonia-induced astrocyte swelling. *J. Biol. Chem.* **283**, 33874–33882 (2008).
5. Ip, Y.K. & Chew, S.F. Ammonia production, excretion, toxicity, and defense in fish: a review. *Front. Physiol.* **1**, 134 (2010).
6. Marcaggi, P., Jeanne, M. & Coles, J.A. Neuron-glial trafficking of $NH4^+$ and K^+: separate routes of uptake into glial cells of bee retina. *Eur. J. Neurosci.* **19**, 966–976 (2004).
7. Waniewski, R.A. Physiological levels of ammonia regulate glutamine synthesis from extracellular glutamate in astrocyte cultures. *J. Neurochem.* **58**, 167–174 (1992).
8. Yamamoto, Y. *et al.* Risk factors for hyperammonemia in pediatric patients with epilepsy. *Epilepsia* **54**, 983–989 (2013).
9. Ye, X. *et al.* Adenovirus-mediated *in vivo* gene transfer rapidly protects ornithine transcarbamylase-deficient mice from an ammonium challenge. *Pediatr. Res.* **41**, 527–534 (1997).
10. Rangroo Thrane, V. *et al.* Real-time analysis of microglial activation and motility in hepatic and hyperammonemic encephalopathy. *Neuroscience* **220**, 247–255 (2012).
11. Ratnakumari, L., Qureshi, I.A. & Butterworth, R.F. Effects of congenital hyperammonemia on the cerebral and hepatic levels of the intermediates of energy metabolism in spf mice. *Biochem. Biophys. Res. Commun.* **184**, 746–751 (1992).
12. Martinez-Hernandez, A., Bell, K.P. & Norenberg, M.D. Glutamine synthetase: glial localization in brain. *Science* **195**, 1356–1358 (1977).
13. Ratnakumari, L., Audet, R., Qureshi, I.A. & Butterworth, R.F. Na^+,K^+-ATPase activites are increased in brain in both congenital and acquired hyperammonemic syndromes. *Neurosci. Lett.* **197**, 89–92 (1995).
14. Lichter-Konecki, U., Mangin, J.M., Gordish-Dressman, H., Hoffman, E.P. & Gallo, V. Gene expression profiling of astrocytes from hyperammonemic mice reveals altered pathways for water and potassium homeostasis in vivo. *Glia* **56**, 365–377 (2008).
15. Thrane, A.S. *et al.* Critical role of aquaporin-4 (AQP4) in astrocytic Ca^{2+} signaling events elicited by cerebral edema. *Proc. Natl. Acad. Sci. USA* **108**, 846–851 (2011).
16. Thrane, A.S. *et al.* General anesthesia selectively disrupts astrocyte calcium signaling in the awake mouse cortex. *Proc. Natl. Acad. Sci. USA* **109**, 18974–18979 (2012).
17. Stephan, J. *et al.* Kir4.1 channels mediate a depolarization of hippocampal astrocytes under hyperammonemic conditions in situ. *Glia* **60**, 965–978 (2012).
18. Wall, S.M. & Koger, L.M. $NH4^+$ transport mediated by Na^+-K^+-ATPase in rat inner medullary collecting duct. *Am. J. Physiol.* **267**, F660–F670 (1994).
19. Nicholson, C. Ion-selective microelectrodes and diffusion measurements as tools to explore the brain cell microenvironment. *J. Neurosci. Methods* **48**, 199–213 (1993).
20. DeSalvo, M.N. *et al.* Focal BOLD fMRI changes in bicuculline-induced tonic-clonic seizures in the rat. *Neuroimage* **50**, 902–909 (2010).
21. Wang, F. *et al.* Astrocytes modulate neural network activity by Ca^{2+}-dependent uptake of extracellular K. *Sci. Signal.* **5**, ra26 (2012).
22. Xiong, Z.Q. & Stringer, J.L. Sodium pump activity, not glial spatial buffering, clears potassium after epileptiform activity induced in the dentate gyrus. *J. Neurophysiol.* **83**, 1443–1451 (2000).
23. Lux, H.D. Ammonium and chloride extrusion: hyperpolarizing syntaptic inhibition in spinal motor neurons. *Science* **173**, 555–557 (1971).
24. Raabe, W. & Gumnit, R.J. Disinhibition in cat motor cortex by ammonia. *J. Neurophysiol.* **38**, 347–355 (1975).
25. Szerb, J.C. & Butterworth, R.F. Effect of ammonium ions on synaptic transmission in the mammalian central nervous system. *Prog. Neurobiol.* **39**, 135–153 (1992).
26. Dzhala, V.I. *et al.* NKCC1 transporter facilitates seizures in the developing brain. *Nat. Med.* **11**, 1205–1213 (2005).
27. Koyama, R. *et al.* GABAergic excitation after febrile seizures induces ectopic granule cells and adult epilepsy. *Nat. Med.* **18**, 1271–1278 (2012).
28. Borgdorff, A.J., Poulet, J.F. & Petersen, C.C. Facilitating sensory responses in developing mouse somatosensory barrel cortex. *J. Neurophysiol.* **97**, 2992–3003 (2007).
29. Rivera, C. *et al.* The K^+/Cl^- co-transporter KCC2 renders GABA hyperpolarizing during neuronal maturation. *Nature* **397**, 251–255 (1999).
30. Hübner, C.A. *et al.* Disruption of KCC2 reveals an essential role of K-Cl cotransport already in early synaptic inhibition. *Neuron* **30**, 515–524 (2001).
31. Delpire, E., Lu, J., England, R., Dull, C. & Thorne, T. Deafness and imbalance associated with inactivation of the secretory Na-K-2Cl co-transporter. *Nat. Genet.* **22**, 192–195 (1999).
32. Flagella, M. *et al.* Mice lacking the basolateral Na-K-2Cl cotransporter have impaired epithelial chloride secretion and are profoundly deaf. *J. Biol. Chem.* **274**, 26946–26955 (1999).
33. Raabe, W.A. Ammonia and disinhibition in cat motor cortex by ammonium acetate, monofluoroacetate and insulin-induced hypoglycemia. *Brain Res.* **210**, 311–322 (1981).
34. Huberfeld, G. *et al.* Perturbed chloride homeostasis and GABAergic signaling in human temporal lobe epilepsy. *J. Neurosci.* **27**, 9866–9873 (2007).
35. Hannaert, P., Alvarez-Guerra, M., Pirot, D., Nazaret, C. & Garay, R.P. Rat NKCC2/NKCC1 cotransporter selectivity for loop diuretic drugs. *Naunyn Schmiedebergs Arch. Pharmacol.* **365**, 193–199 (2002).
36. Benjamin, A.M. Effects of ammonium ions on spontaneous action potentials and on contents of sodium, potassium, ammonium, and chloride ions in brain *in vitro*. *J. Neurochem.* **30**, 131–143 (1978).
37. Dzhala, V.I. *et al.* Progressive NKCC1-dependent neuronal chloride accumulation during neonatal seizures. *J. Neurosci.* **30**, 11745–11761 (2010).
38. Kanaka, C. *et al.* The differential expression patterns of messenger RNAs encoding K-Cl cotransporters (KCC1,2) and Na-K-2Cl cotransporter (NKCC1) in the rat nervous system. *Neuroscience* **104**, 933–946 (2001).
39. Javaheri, S., Davis, C. & Rogers, D.H. Ionic composition of cisternal CSF in acute respiratory acidosis: lack of effect of large dose bumetanide. *J. Neurochem.* **61**, 1525–1529 (1993).

ONLINE METHODS

Mice and breeding. *Otc*$^{spf\text{-}ash}$ B6C3-F1, *Glt1*-eGFP BAC, *Slc12a2*$^{-/-}$ SVJ129/blksw and *Aqp4*$^{-/-}$ C57BL/6J mice were bred as described previously[9,15,32,40]. For *in vivo* experiments, males from 8–12 weeks of age were used. *Otc*$^{spf\text{-}ash}$ mice were crossed with *Glt1*-eGFP mice for imaging experiments. Wild-type littermates of the appropriate strain were either bred or obtained from Jackson Laboratories, along with Wistar rat pups (for neuronal cell cultures). All animal experiments were approved by the Animal Care and Use Committee of the University of Rochester.

Behavioral characterization. We developed a phenotype severity score to quantify the degree of ammonia neurotoxicity based on previous studies[9,41,42]. Each animal was scored every 5–15 min for the following phenotypes: hyperacusis (0–2), imbalance (0–3), ataxia/tremor (0–3) and level of consciousness (0–3). A maximum score of 11 represents deep coma (no corneal reflex), whereas 0 represents normal wakefulness. Hyperacusis was scored as 0 if the mouse did not display a startle response to 30–60 dB sound, 1 if the mouse responded to only 60 dB and 2 if it responded to 30 dB, too. Imbalance was scored using a ledge test, and the mice were given a score of 0 if they balanced on the ledge and let themselves down in a controlled fashion, 1 if they lost their footing while walking on the ledge, 2 if they did not effectively walk on or let themselves down from the ledge and 3 if they were unable to walk or get down from the ledge or simply fell off. Ataxia/tremor was scored using a gait test, where the mouse was encouraged to walk for a short distance. The mouse was scored 0 if it walked effectively, 1 if it had a slight tremor, 2 if it had a broad- based gait or severe tremor and 3 if it dragged its abdomen on the ground or was unable to walk. Consciousness was scored as 0 for awake, 1 for loss of scatter reflex, 2 for loss of righting reflex (LORR) and 3 for loss of corneal reflex. Automated movement analysis was performed using AnyMaze software analysis of CCD-camera recordings in a standard mouse cage. To analyze cognitive abilities, two commercial conditioning chambers (H10-11M-TC, Coulbourn Instruments) were adapted for contextual fear conditioning. Over the course of 4 d, mice were trained via a tone/shock protocol and trained to fear contextual and auditory cues[43–45]. Better-trained mice exhibited higher percentages of time during a 5-min trial freezing in the presence of auditory or contextual cues.

Animal preparation for awake *in vivo* recordings. Mouse preparation was modified from published protocols[10,46]. Briefly, mice were anesthetized using isoflurane (1.5% mixed with 1–2 L min^{-1} O_2), head restrained with a custom-made miniframe and habituated to the restraint over 2 d in multiple sessions, with a total training duration of 3–4 h. A 1.5-mm craniotomy was then opened over the somatosensory cortex (1.5 mm in diameter, 3 mm lateral and 1.5 mm posterior to the bregma), the dura was carefully removed and the mice were allowed 60 min recovery before conducting the experiments. The craniotomy procedure lasted <20 min to minimize anesthesia exposure on the recording day. Animals were then head-restrained, placed in a behavioral tube to minimize movement and relocated to the imaging room, which was kept dark and quiet. Body temperature was maintained with a heating pad. For systemic drug treatment, a polyethylene intraperitoneal (i.p.) catheter was surgically implanted using a Seldinger technique to deliver drugs accurately and with minimal manipulation. For cortical drug application, artificial cerebrospinal fluid (aCSF) was perfused across the cortex of awake mice at a rate of 2 mL min^{-1}, into a custom-made well with ~200 µL volume, through tubing with ~100 µL volume, meaning the entire volume bathing the brain was exchanged every ~9 s. The aCSF solution contained (in mM) 126 NaCl, 2.5 KCl, 1.25 NaH_2PO_4, 2 $MgCl_2$, 2 $CaCl_2$, 10 glucose and 26 $NaHCO_3$, pH 7.4. For imaging, calcium indicator rhod-2 AM (Invitrogen, 2 mM) was loaded onto exposed cortex for 30–40 min before application of agarose (1.5%, type III-A, Sigma) and a coverslip[15].

Electrophysiological recordings. *In vivo* and *in situ* recordings were obtained from layer II somatosensory cortex, and coronal cortical slices were prepared from mice at 21–30 d after birth. Ion-sensitive microelectrodes (ISMs) for K^+, $NH4^+$ and H^+ were pulled from double-barreled pipette glass (PB150-6, WPI) with a tip diameter of 1–3 µm. The pipettes were silanized (coated) with dimethylsilane I (Fluka, Sigma) and filled with either K^+ ionophore I cocktail B (Fluka, selectivity coefficient −1.8 log(K^+/NH_4^+)), $NH4^+$ ionophore I cocktail B (Fluka, −0.9 log(NH_4^+/K^+)) or H^+ ionophore I cocktail A (Fluka, Sigma). The backfill solutions for the K^+, $NH4^+$ and H^+ ISMs were 0.15 M KCl, 0.5 M NH_4Cl and phosphate-buffered saline (PBS) with a pH of 7.4, respectively. The reference barrels were used to record the DC potentials and were filled with 0.15 M NaCl. In selected experiments, single-barrel electrodes were also used in combination with single-reference electrodes placed within 50 µm of each other. All ISMs were calibrated before and after each experiment using standard solutions (a <5% difference was acceptable), and the calibration data were fitted to the Nikolsky equation to determine electrode slope and interference[19]. K^+ and NH_4^+ ISM traces were subtracted for ionic interference calculated by cross-calibrating the electrodes before use[17]. K^+ calibrations were done in 150 mM NaCl that contained doubling steps of K^+ over a range of concentrations appropriate for the experiment, usually 3–48 mM. $NH4^+$ calibrations were carried out in 150 mM NaCl and aCSF from 0.1 mM to 10 mM to determine the sensitivity during the *in vivo* environment. H^+ calibrations were carried out in phosphate buffers from pH 5 to pH 9, where >90% had a response time of 1–5 s and a 51- to 59-mV response to 1 pH unit change.

Whole-cell and gramicidin perforated patch-clamp recordings were performed as described previously[27,47]. Briefly, for whole-cell recordings we used electrodes with 3–5 MΩ resistance and an intracellular solution containing 135 mM K-methylsulfate, 10 mM KCl, 10 mM HEPES, 5 mM NaCl, 2.5 mM Mg-ATP, 0.3 mM Na-GTP (pH 7.3) and Alexa Fluor 350 (Invitrogen). Gramicidin perforated patch electrodes were filled with stock gramicidin (Sigma, 25 mg ml^{-1} in DMSO), which was diluted to a final concentration of 50 µg ml^{-1} in solution containing 130 mM KCl, 5 mM NaCl, 0.4 mM $CaCl_2$, 1 mM $MgCl_2$, 1.1 mM EGTA and 10 mM HEPES. Electroencephalogram (EEG) signals were externally filtered at 6 Hz (Filter Butterworth Model by Encore, Axopatch 200B by Axon Instruments), bandpass filtered at 1–100 Hz and digitized (Digidata 1440A by Axon Instruments). ISM signals were amplified (FD223a by WPI) and externally filtered and digitized as above, and reference field potential traces were subtracted. In selected experiments, wireless electromyogram (EMG) and electroencephalogram (EEG) electrodes were implanted (DSI Physiotel), and an extracellular microelectrode was placed in the thalamus (ventrobasal complex). Recordings were analyzed offline using pClamp 10.2. Myoclonic seizures were defined on the EEG as single or multiple 3–9 Hz polyspike and wave discharges (SWD) of 0.2–2 s duration associated with myoclonic jerks determined by video recording, EMG and direct observation. Whisker stimulation was delivered using a picospritzer III (Parken Instrumentation) and Master 8 (A.M.P.I.). Stimuli consisted of paired 50-µs air pulses with an interstimulus interval of 150 ms, and paired-pulse ratio (PPR) was calculated as previously described[28]. All solutions were pH (7.4) and osmolarity adjusted.

Two-photon laser scanning microscopy. A Mai Tai laser (SpectraPhysics) attached to a confocal scanning system (Fluoview 300, Olympus) and an upright microscope (IX51W) was used. *In vivo* volume changes and calcium activity were imaged in the cortex 100 µm below the pial surface as described before[15,16], using 60× (1.1NA) and 20× (0.95NA) lenses, respectively. For *in vivo* volumetry, we collected XYZT image series (*z* step 1.5 µm, every 5 min) with acquisition time <20 s and laser power <40 mW. For *in vivo* calcium imaging, we collected dual-channel (rhod-2 and eGFP) frames at 0.2 or 1 Hz. A low sampling rate and <20 mW laser were also used here to avoid photodamage. A calcium transient was defined as an event where the relative ratio between the rhod-2 and eGFP signal intensities ($\Delta F/F_0$) was >2 s.d. (σ) from baseline. Beginning and end were defined as $\Delta F/F_0 > 0.5\ \sigma$ and $< 0.5\ \sigma$, respectively. Amplitude was taken as the peak $\Delta F/F_0$ in this interval. For *in situ* volumetric imaging, acute cortical slices were loaded with Texas red hydrazide (1.5 µM, a fixable sulforhodamine 101 derivative) in aCSF for 50 min. Volume and calcium recordings were analyzed using previously described custom-made software (Matlab)[15].

Cell culture assays. Cultured neocortical astrocytes and neurons were prepared from mouse and rat pups, respectively, 1–2 d after birth as previously described[21,48]. For $^{86}Rb^+$ experiments, the cultures were incubated for 10 min with or without ouabain (1 mM). The potassium analog $^{86}Rb^+$ was then added

to each well plate for 15 min in the presence of different NH_4Cl concentrations (0–10 mM) (1 μCi, PerkinElmer). The reaction was stopped by placing the cells on ice and washing with ice-cold aCSF. The cells were lysed, and $^{86}Rb^+$ uptake was quantified by liquid scintillation counting (Beckman Coulter). For Na^+-K^+ ATPase activity, astrocyte cultures were used as previously described, and enzyme activity was quantified using the malachite green reaction (Sigma) and analyzed using spectrophotometry[49].

Immunohistochemistry. Mice were anesthesized and perfused transcardially with 4% paraformaldehyde, and the brains were post-fixed overnight. Serial 16-μm sagittal cryostat sections were cut after overnight cryoprotection in 30% sucrose. Sections were incubated with goat anti-NKCC1 primary antibody (1:200, Santa Cruz Biotechnology, sc-21547) overnight at 4 °C, followed by incubation with an Alexa-488–conjugated donkey anti-goat secondary antibody (1:500, Invitrogen, A-11055). Vectashield containing DAPI (Vector) was used for mounting. Images were taken with a 10× lens in a BX53 Olympus system microscope attached to a DP72 Olympus digital camera.

Biochemical and hemodynamic analyses. Plasma ammonia analysis was performed on blood samples collected using 50-μL heparinized tubes from the femoral artery. An L-glutamate dehydrogenase–based kit (Sigma) was used for the quantification of ammonia in plasma[50]. For hemodynamic recordings, an intracranial pressure probe (Millar) was inserted through a small 0.5-mm craniotomy over the somatosensory cortex. Cerebral blood flow was assessed using a fiberoptic laser Doppler probe (PF5010, Perimed) and connected to an infrared laser Doppler flowmeter[51]. Blood pressure was monitored through the femoral artery cannula (SYS-BP1, WPI), and cerebral perfusion pressure was deduced by subtracting ICP from blood pressure[52]. All signals were digitized (Digidata 1332A, Axon Instruments) and analyzed (pClamp 10.2). Brain water content was assessed using wet-to-dry ratios of brain weight as described previously[53]. For ^{1}H-NMR, mouse forebrains were extracted, frozen with liquid nitrogen and homogenized in 7.5 mL 12% PCA at 0 °C using a microsonicator. The homogenate was centrifuged at 25,000*g* for 15 min, and the supernatants were neutralized to pH 7.0 with KOH over an ice bath. A further 15-min centrifugation (25,000*g*) separated the resultant $KClO_4$, and the supernatant was lyophilized before being reconstituted with 0.65 ml deuterated water, as described previously[54]. ^{1}H-NMR spectra were acquired at 25 °C using a 600-mHz Varian UnityINOVA spectrometer equipped with a triple-axis gradient HCN probe. Signals were acquired following a 90° pulse with a 7,200 Hz spectral width and 32,000 data points. The time between pulses was 15 s, and 64 signals were averaged for each spectrum. Integrals of the relevant peaks were converted to μmol/g wet weight and normalized to NAA (methyl) to increase intersample consistency.

Statistical analyses. All analyses were performed using SPSS 19 software (IBM), and all tests were two-tailed where significance was achieved at $\alpha = 0.05$ level. Where $n \geq 10$ for normally distributed data, an unpaired *t* test (fewer than or equal to two variables) or ANOVA (more than two variables) were used for independent samples, and paired *t* test for paired samples. Where $n < 10$ or the data were non-normally distributed, we employed nonparametric tests including Mann-Whitney *U* (fewer than or equal to two variables) or Kruskall-Wallis (more than two variables) for independent samples and Wilcoxon signed-ranks test for paired samples. Overdose survival was compared using a Cox regression model (controlling for the potential confounding effect of mouse weight and age).

40. Regan, M.R. *et al.* Variations in promoter activity reveal a differential expression and physiology of glutamate transporters by glia in the developing and mature CNS. *J. Neurosci.* **27**, 6607–6619 (2007).
41. Guyenet, S.J. *et al.* A simple composite phenotype scoring system for evaluating mouse models of cerebellar ataxia. *J. Vis. Exp.* **1787** (2010).
42. Matkowskyj, K.A. *et al.* Azoxymethane-induced fulminant hepatic failure in C57BL/6J mice: characterization of a new animal model. *Am. J. Physiol.* **277**, G455–G462 (1999).
43. Han, X. *et al.* Forebrain engraftment by human glial progenitor cells enhances synaptic plasticity and learning in adult mice. *Cell Stem Cell* **12**, 342–353 (2013).
44. Anagnostaras, S.G., Josselyn, S.A., Frankland, P.W. & Silva, A.J. Computer-assisted behavioral assessment of Pavlovian fear conditioning in mice. *Learn. Mem.* **7**, 58–72 (2000).
45. Wiltgen, B.J. & Silva, A.J. Memory for context becomes less specific with time. *Learn. Mem.* **14**, 313–317 (2007).
46. Dombeck, D.A., Khabbaz, A.N., Collman, F., Adelman, T.L. & Tank, D.W. Imaging large-scale neural activity with cellular resolution in awake, mobile mice. *Neuron* **56**, 43–57 (2007).
47. Wang, F., Xiao, C. & Ye, J.H. Taurine activates excitatory non-synaptic glycine receptors on dopamine neurones in ventral tegmental area of young rats. *J. Physiol. (Lond.)* **565**, 503–516 (2005).
48. Lin, J.H. *et al.* Gap-junction-mediated propagation and amplification of cell injury. *Nat. Neurosci.* **1**, 494–500 (1998).
49. Anupama Adya, H.V. & Mallick, B.N. Comparison of Na-K ATPase activity in rat brain synaptosome under various conditions. *Neurochem. Int.* **33**, 283–286 (1998).
50. Mondzac, A., Ehrlich, G.E. & Seegmiller, J.E. An enzymatic determination of ammonia in biological fluids. *J. Lab. Clin. Med.* **66**, 526–531 (1965).
51. Takano, T. *et al.* Cortical spreading depression causes and coincides with tissue hypoxia. *Nat. Neurosci.* **10**, 754–762 (2007).
52. Ren, Z. *et al.* 'Hit & Run' model of closed-skull traumatic brain injury (TBI) reveals complex patterns of post-traumatic AQP4 dysregulation. *J. Cereb. Blood Flow Metab.* **33**, 834–845 (2013).
53. Haj-Yasein, N.N. *et al.* Glial-conditional deletion of aquaporin-4 (Aqp4) reduces blood-brain water uptake and confers barrier function on perivascular astrocyte endfeet. *Proc. Natl. Acad. Sci. USA* **108**, 17815–17820 (2011).
54. Zwingmann, C., Chatauret, N., Leibfritz, D. & Butterworth, R.F. Selective increase of brain lactate synthesis in experimental acute liver failure: results of a [^{1}H–^{13}C] nuclear magnetic resonance study. *Hepatology* **37**, 420–428 (2003).

doi:10.1038/nm.3400